AFRL-OSR-VA-TR-2013-0011

Silicon Based Colloidal Quantum Dot and Nanotube Lasers

Bhattacharya, P., Heo, J., Bhowmick, S.

University of Michigan

March 2013
Final Report

AIR FORCE RESEARCH LABORATORY
AF OFFICE OF SCIENTIFIC RESEARCH (AFOSR)
ARLINGTON, VIRGINIA 22203
AIR FORCE MATERIEL COMMAND

REPORT DOCUMENTATION PAGE

1. REPORT DATE (DD-MM-YYYY)	2. REPORT TYPE	3. DATES COVERED (From - To)
13-09-2012	FINAL	9/1/2009 to 8/31/2012

4. TITLE AND SUBTITLE

Silicon Based Colloidal Quantum Dot and Nanotube Lasers

5a. CONTRACT NUMBER

5b. GRANT NUMBER

FA9550-09-1-0634

5c. PROGRAM ELEMENT NUMBER

6. AUTHOR(S)

Professor Pallab Bhattacharya, Junseok Heo, Sishir Bhowmick

5d. PROJECT NUMBER

5e. TASK NUMBER

5f. WORK UNIT NUMBER

7. PERFORMING ORGANIZATION NAME(S) AND ADDRESS(ES)

University of Michigan

8. PERFORMING ORGANIZATION REPORT NUMBER

9. SPONSORING/MONITORING AGENCY NAME(S) AND ADDRESS(ES)

AFOSR/RSE
875 N Randolph St
Arlington, VA 22203

10. SPONSOR/MONITOR'S ACRONYM(S)

11. SPONSOR/MONITOR'S REPORT NUMBER(S)

AFRL-OSR-VA-TR-2013-0011

12. DISTRIBUTION/AVAILABILITY STATEMENT

Distribution A: Approved for Public Release

13. SUPPLEMENTARY NOTES

14. ABSTRACT

The most significant accomplishments in this project are: (a) demonstration of optically pumped quantum dot rolled-up microtube lasers with the minimum linewidth of 0.8 nm. After considering radiation, bending and substrate losses associated with the devices, the threshold carrier density is theoretically and experimentally derived to be inversely proportional to the diameter; (b) demonstration of InGaN/ GaN light emitting diodes and GaN single nanowire photonic crystal laser on silicon characterized by a lasing transition at $\lambda=371.3$ nm with a linewidth of 0.55 nm. The threshold is observed at a pump power density of ~120 kW/cm2 and the spontaneous emission factor β is estimated to be 0.08; (c) demonstration of lasing at ~1.55 μm with PbSe quantum dots (QDs) on silicon. The measured electroluminescence exhibits a minimum linewidth of ~3.1 nm at a low injection current density of 3 A/cm2, and highly directional emission characteristics; (d) investigation of role of polariton-electron scattering and magnetic field on the performance characteristics of an e

15. SUBJECT TERMS

16. SECURITY CLASSIFICATION OF:			17. LIMITATION OF ABSTRACT	18. NUMBER OF PAGES	19a. NAME OF RESPONSIBLE PERSON
a. REPORT	b. ABSTRACT	c. THIS PAGE			Professor Pallab Bhattacharya
U	U	U	U		19b. TELEPHONE NUMBER (Include area code)
					000-000-0000

Reset

Standard Form 298 (Rev. 8/98)
Prescribed by ANSI Std. Z39.18

FINAL REPORT

To: technicalreports@afosr.af.mil and
Program Manager Dr. Gernot S. Pomrenke — gernot.pomrenke@afosr.af.mil

From: Professor Pallab Bhattacharya, University of Michigan, EECS/SSEL
Subject: FINAL REPORT (AFOSR FA9550-09-1-0634)
Date: September 13, 2012

Contract/Grant Title: Silicon Based Colloidal Quantum Dot and Nanotube Lasers
Contract/Grant #: FA9550-09-1-0634
Reporting Period: 9/1/2009 to 8/31/2012

Personnel: Professor Pallab Bhattacharya, Junseok Heo, Sishir Bhowmick

Significant Accomplishments:

The most significant accomplishments in this project are: (a) demonstration of optically pumped quantum dot rolled-up microtube lasers with the minimum linewidth of 0.8 nm. After considering radiation, bending and substrate losses associated with the devices, the threshold carrier density is theoretically and experimentally derived to be inversely proportional to the diameter; (b) demonstration of InGaN/ GaN light emitting diodes and GaN single nanowire photonic crystal laser on silicon characterized by a lasing transition at λ=371.3 nm with a linewidth of 0.55 nm. The threshold is observed at a pump power density of ~120 kW/cm^2 and the spontaneous emission factor β is estimated to be 0.08; (c) demonstration of lasing at ~1.55 μm with PbSe quantum dots (QDs) on silicon. The measured electroluminescence exhibits a minimum linewidth of ~3.1 nm at a low injection current density of 3 A/cm^2, and highly directional emission characteristics; (d) investigation of role of polariton-electron scattering and magnetic field on the performance characteristics of an electrically injected GaAs-based quantum well microcavity diode in the strong coupling. An electron gas is introduced in the quantum wells by modulation doping with silicon dopants. It is observed that polariton-electron scattering suppresses the relaxation bottleneck in the lower polariton branch.

1. Quantum Dot Rolled-up Microtube Lasers

The rolled-up microtube is formed by strain mismatch between two semiconductor layers. The basic structure is shown in Fig. 1. As the AlAs sacrificial layer is etched away, the rolling process starts and a complete rotation takes place. Coherent emission from the rolled-up microtube is obtained by inserting quantum wells or dots in the bilayers. We demonstrated relatively simplified calculation of the losses and the threshold condition, and the measured dependence of the threshold power on the diameter of InAs QD microtube lasers. The spectral emission characteristics of these devices have also been analyzed.

The device heterostructure, grown by molecular beam epitaxy (MBE), is shown in the left inset of Fig. 1(a). Two layers of InAs QDs are inserted in the GaAs layer. To

fabricate rolled-up free standing microcavities, a U-shaped mesa is first defined by selectively etching down to the InGaAs layer with a H_2O_2/H_3PO_4 mixture where the ending edge of the U-Shaped body is either straight or has corrugation. The starting edge of rolling is defined by deep etching through the AlAs sacrificial layer with the same solution. The self-rolling process is initiated as the diluted hydrofluoric (HF) acid solution undercuts the InGaAs layer. The central part of the tube is suspended due to the U-shaped mesa, as seen in the photo-micrograph of Fig. 1(b). The scanning electron microscopy image of a quantum dot microtube with a corrugated notch is shown in the inset of Fig. 1(b).
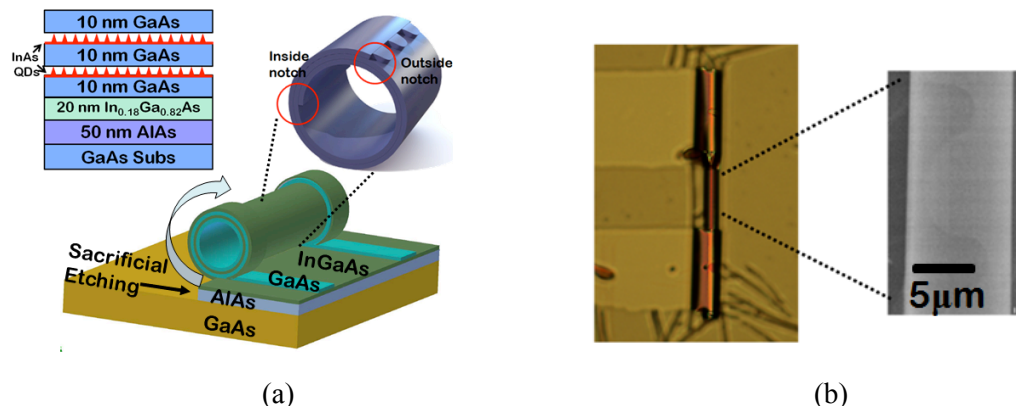

(a)   (b)

Figure 1 (a) Schematic representation of a free-standing rolled-up microtube. The left inset shows heterostructure of device with two layers of InAs quantum dots buried in the GaAs matrix. The bridge part of the microtube is schematically magnified in the right inset. It shows the inside and outside notches and the corrugation at the outside notch; (b) optical microscopy image of a fabricated rolled-up microtube showing the suspended bridge. The scanning electron microscopy (SEM) in the inset shows the corrugation in the bridge region of the microtube.

The emission characteristics of the QD microtube devices were determined by micro-photoluminescence (PL) measurements. The excitation from a diode laser ($\lambda = 523$ nm) was focused to a 20 µm illumination area on the microtube with the use of a suitable objective lens. All measurements have been made with the samples at room temperature. Excitation dependent micro-PL spectra and output light intensity from a rolled-up microtube of 9 µm diameter and ~130 nm wall thickness, separated from the substrate by ~400 nm, are shown in Fig. 2(a) and (b), respectively. A microtube cavity can support an azimuthal mode propagating along the circumference with the E-field along the axial direction. The sharp peaks observed in the emission spectra of Fig. 2(a) are identified to be the azimuthal modes separated by ~18 meV which satisfy the phase matching condition of a ring resonator given by: $\pi D n_{eff} = \lambda m$. Here D, n_{eff}, λ, and m are, respectively, the tube diameter, effective refractive index of the bi-layer, resonant wavelength and the azimuthal mode number. It is worth noting that the lasing threshold is different for different azimuthal modes in the same device. In a 9 µm diameter microtube, the 64th azimuthal mode exhibits the lowest threshold, as depicted in Fig. 2(b). The different lasing threshold for various azimuthal modes contributes to the wavelength dependent loss in microtubes and gain curves in InAs QDs.
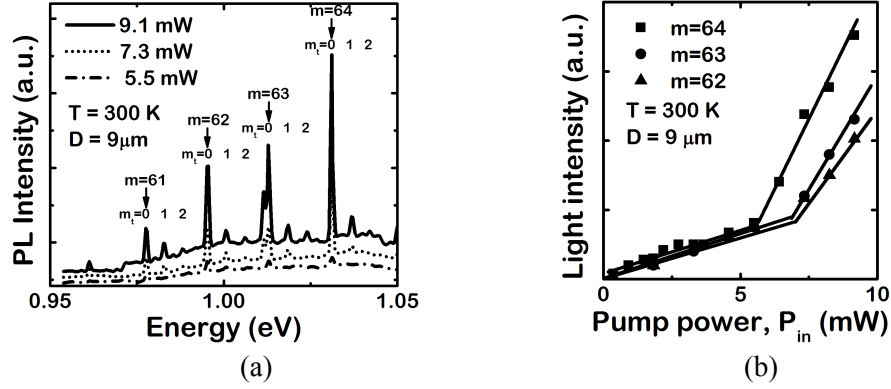
Figure 2 (a) Room-temperature micro-photoluminescence spectra from the rolled-up microtube device of diameter ~9 µm for different incident powers; (b) output light intensity versus incident pump power for different azimuthal modes in the same microtube.

In order to understand the role of various losses and of a key parameter, the diameter of the microtube, on the threshold behavior of the laser, we have formulated and calculated the modal gain and derived the analytical form of the important losses. The threshold condition is then obtained. The gain of the devices investigated in this study is provided by a couple of layers of InAs self- organized quantum dot layers. The dots are generally assumed to be of pyramidal shape with base diameter and height of 20-30 nm and 6-7 nm, respectively. The dot density (N_{qd}) is ~5×10^{10} cm^{-2}. Inhomogeneous and homogeneous broadening was taken into account in calculation. The calculated modal gain of the QD active region revealed that the transparency carrier density is ~7×10^{10} cm^{-2} and saturation is observed for n $\geq 4\times10^{11}$ cm^{-2}.
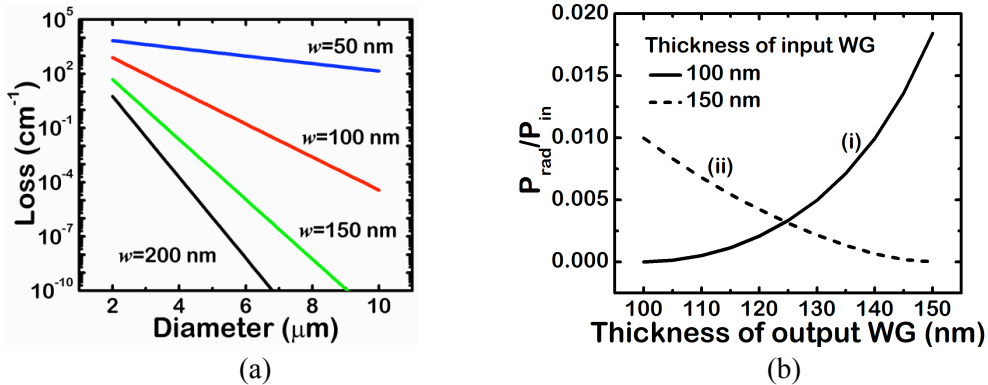

Figure 3 (a) Calculated bending loss as a function of diameter for different wall thicknesses; (b) radiation loss as a function of output waveguide thickness.

In order to derive the threshold condition, the microtube is approximated as a ring resonator consisting of two different wall thicknesses, w_1 and w_2 and two notches, inside and outside. Since the wall thickness is much smaller than the microtube diameter, a uniform diameter of D is assumed. The losses in the microtube are the bending loss α_{bend} while light travels along the curvature of the tube circumference, radiation loss R_n (= 1 - T_n), where T_n is the transmission, at the notches due to the step discontinuities, and optical loss into the substrate. The change in the light intensity after one round trip is then expressed as:

3

$$I = I_0 T_1 T_2 \exp[(\Gamma g - \alpha_{bend1})l_1 + (\Gamma g - \alpha_{bend2})l_2 - \alpha_{sub}l] = I_0 \qquad (1)$$

where $l_1 = D(\pi\phi)$, $l_2 = D\phi/2$ and $l = l_1 + l_2$. α_{bend1} and α_{bend2} are bending losses in the microtube section of thickness w_1 and w_2, respectively, and α_{sub} is the substrate loss. The threshold condition is then expressed as:

$$\Gamma g_{th} = \frac{\alpha_{bend1}l_1 + \alpha_{bend2}l_2}{l} + \frac{1}{l}\ln\left(\frac{1}{T_1 T_2}\right) + \alpha_{sub} \qquad (2)$$

where Γg_{th} is the modal gain at threshold.

The wave equation in cylindrical coordinates for a wave propagating along the circumference is solved to evaluate the bending loss, which is the ratio of radiated power to the total power. The bending loss is plotted in Fig. 3(a) for different microtube wall thickness values and is evident that $\alpha_{bend} \propto exp(-D)$. A wave traveling along the circumference of the microtube experiences step discontinuities at the two notches and there is radiation of power. This is modeled as a straight waveguide with a step discontinuity. By invoking mode matching and energy conservation at the steps, the radiation rate can be evaluated. The calculated scattering losses as a function of output waveguide thickness are depicted in Fig. 3(b). The curves (i) and (ii) represent scattering losses for the wave traveling from a wall with $w = 100$ nm to the wall of larger w, and in travelling from a wall with $w = 150$ nm to the wall of smaller w, respectively. It is evident that for a rolled-up microtube with wall thickness $w_1 = 100$ nm and $w_2 = 150$ nm, the rate of radiation at the two notches are $R_1 = 0.01$ and $R_2 = 0.08$, knowing that $T_1 = 1 - R_1$ and $T_2 = 1 - R_2$. We also have evaluated the substrate loss and found out it can be ignored for larger separation, as is the case of the devices fabricated for this study (~ 0.5 µm).
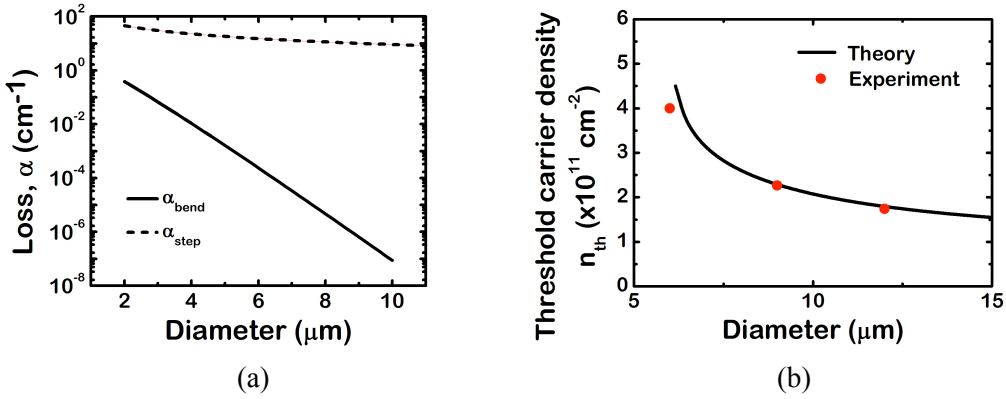

Figure 4 (a) Comparison of radiation loss at a step notch and bending loss in the microtube cavity as a function of tube diameter; (b) variation of threshold carrier density in active region of the lasers with microtube diameter.

The calculated bending and radiation losses are compared in Fig. 4(a) for microtubes of varying diameters. The bending loss becomes important only for very small diameter microtubes. Therefore for the microtubes fabricated and characterized in the present study, the dominant loss mechanism is scattering and radiation at the notches. The threshold condition then becomes simplified shown below.

$$\Gamma g_{th} \cong \frac{1}{\pi D}\ln\left(\frac{1}{T_1 T_2}\right) \qquad (3)$$

The measured output light intensity versus pump power for QD microtube lasers of varying diameter are compared. In order to avoid any wavelength dependent variation,

the azimuthal modes with the similar wavelength for each device have been chosen for comparison. The threshold carrier density in the quantum dots is obtained from the incident and absorbed power for each device and is plotted as a function of device diameter in Fig. 4(b). The solid line is the calculated trend, using the variation of modal gain with tube diameter and with carrier density in the active region and there is an excellent agreement between the two sets of data. The threshold carrier density in the active region is therefore inversely proportional to the microtube diameter

2. InGaN/GaN Nanowire Light Emitting Diodes and Single GaN Nanowire Laser on Silicon

Catalyst-free nanowires were grown on (001) silicon substrate by plasma-assisted MBE. A few monolayers of Ga are first deposited at 800 °C onto the substrate in the absence of nitrogen. To study the growth phenomena, GaN nanowires were grown at 800 °C under different conditions. To achieve different emission wavelengths, InGaN nanowires with varying In compositions were grown under nitrogen rich conditions at 500 – 580 °C. The aerial density of the nanowires can be varied in the range of $10^8 – 10^{11}$ cm^{-2} by varying the duration and magnitude of the initial Ga flux to form the droplets. The structural characteristics of the nanowires were studied using SEM and TEM techniques (Fig. 5).
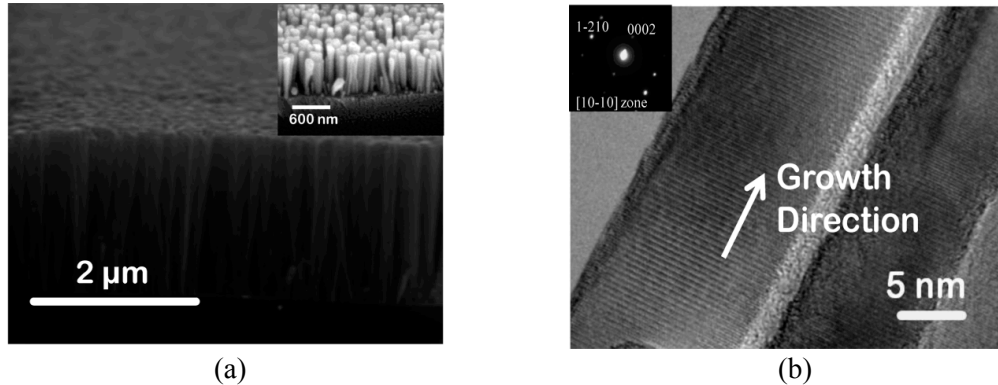

(a)   (b)

Figure 5 (a) Cross-sectional SEM image of catalyst-free InGaN NWs grown by plasma-assisted MBE on (001) Si. The vertically aligned InGaN nanowires are 10 -50 nm in diameter and 2 μm long. The inset oblique view SEM image of n-GaN/InGaN/p-GaN nanowires shows that the nanowires are vertically aligned and separated at the top; (b) HRTEM image of InGaN nanowire of 20 nm diameter. The inset shows the selective area diffraction pattern. Defects are generally not observed.

Light emitting diodes were fabricated with epitaxially grown p-i-n InGaN/GaN green- and "white"-emitting nanowires on n-type (001) silicon. Three hundred nanometers of Si-doped GaN nanowire is first grown followed by 300 nm undoped InGaN with fixed or continuously varied In composition and 150 nm Mg-doped p-type GaN on top. The nanowires were planarized with a parylene-insulating layer and covered by 5 nm/5 nm Ni/Au and 250 nm indium tin oxide as a top ohmic contact on the p-GaN nanowires. Aluminum was deposited on the n-type Si to form the bottom electrode (the inset of Fig. 6(a)).
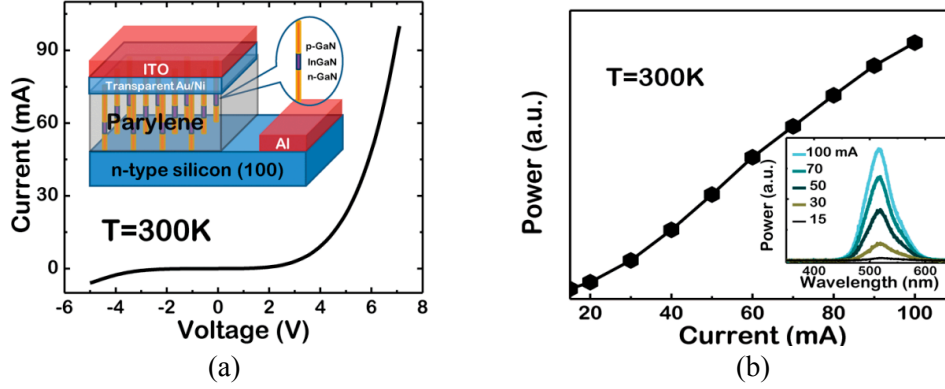
Figure 6 (a) Room temperature current-voltage characteristics of nanowire LEDs. The fabricated device on (001) Si is schematically shown in the inset; (b) measured electroluminescence showing the peak intensity with injection current. The corresponding variation in the output spectrum is shown in the inset. There is no observed shift of the emission peak with increased injection current.

The measured room temperature current-voltage characteristics of the diode is shown in Fig. 6(b). The light-current characteristics shows no saturation up to 100 mA (54 A/cm^2) without any heat-sinking or cooling. The emission peak was at 520 nm with a linewidth of ~50 nm, which did not show any shift with increasing carrier injection, usually observed in InGaN/GaN quantum well or quantum dot heterostructure due to piezoelectricitiy-induced quantum confined Stark effect. Because the active region of the device is bulk InGaN nanowires, quantum confinement is very weak along the growth direction (c-axis). Thus the Stark effect is expected to be very small. The invariant emission peak wavelength with respect to injection current suggests that band-tail filling effect due to compositional inhomogeneity and alloy disorder are negligible.
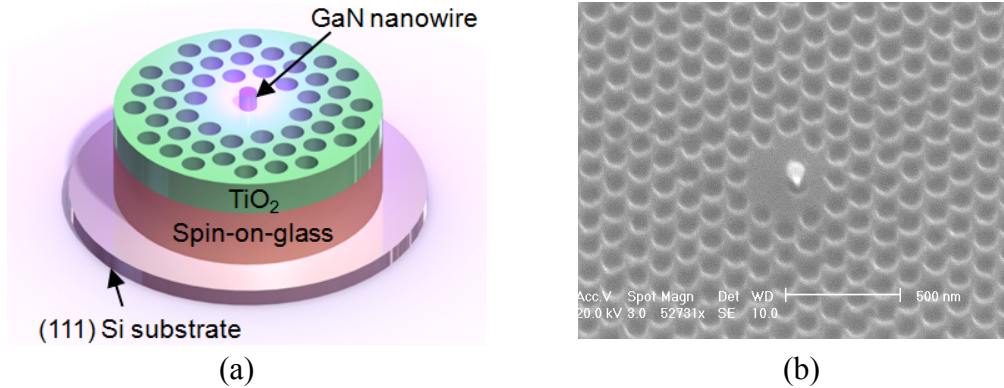

Figure 7 (a) Schematic representation of nanowire laser consisting of a single GaN nanowire and a two dimensional photonic crystal microcavity; (b) an oblique view SEM image of the fabricated device.

The single GaN nanowire photonic crystal laser was demonstrated. The device heterostructure, schematically shown in Fig. 7(a), consists of a single GaN nanowire at the center of a H2 defect and surrounded by a 2D PC microcavity fabricated in a TiO$_2$ layer and a spin-on-glass (SOG) layer as a low refractive index material to reduce optical loss from the TiO$_2$ layer to the Si substrate. As a resonator, a H2 defect PC microcavity is chosen to tolerate any alignment error in a lithography step and is designed by using

three-dimensional (3D) finite difference time domain (FDTD) simulation. The PC is formed with a triangular lattice of air holes of radius 40 nm and period 120 nm. As shown in Fig. 7(b), a small hollow that is formed around the nanowire in the center of the H2 defect during device fabrication. The depth of the hollow was roughly estimated to be ~30 nm based on the amount of TiO_2 deposited on top of nanowire. The calculated Q-factor, mode volume, and confinement factor Γ, obtained from the FDTD simulation, are 570, ~0.003223 μm^3 (0.92$(\lambda/n)^3$), and 0.04, respectively. The modal gain estimated from the Q-factor is ~520 cm^{-1} and the corresponding optical gain at threshold is ~13000 cm^{-1}, which is achievable in GaN.
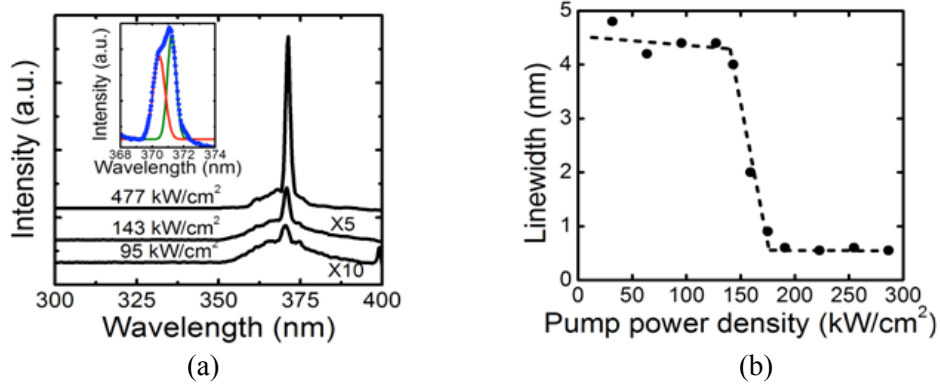

Figure 8 (a) Photoluminescence of the laser at pump power densities of 95 kW/cm2 (below threshold), 143 kW/cm2 (near threshold) and 477 kW/cm2 (above threshold). Spectra are offset for clarity. The inset shows the lasing spectrum (blue circles), which is matched to the sum of two Gaussian peaks (green and red solid lines); (b) measured linewidth of the dominant peak as a function of the pump power density.

The device is optically excited at room temperature with a pulsed laser at λ=266 nm with a pulse duration of ~100 fs and a repetition rate of 80 MHz. The pumping laser is focused on the device with an infinity-corrected objective lens (×27) and the emitted light is collected with the same lens. The output spectrum is analyzed with a monochromator (resolution ~0.5 nm) and detected with a photomultiplier tube using phase lock-in amplification. Figure 8(a) shows the output spectra recorded for pump power densities of 95 kW/cm^2 (below threshold), 143 kW/cm^2 (slightly above threshold), and 477 kW/cm^2 (above threshold). At low pump power density (~95 kW/cm^2), a broad GaN bandedge emission with a full width at half maximum (FWHM) of ~10 nm is observed, which compares well with the reported linewidth of ~12 nm for GaN bandedge emission. The output emission also exhibits a fairly narrow peak (~4.5 nm) at λ=370.4 nm which is believed to be due to the Purcell effect which enhances spontaneous emission. The enhanced spontaneous emission peak becomes more pronounced near threshold (120 kW/cm^2) and evolves into a coherent lasing peak above threshold. The spectrum recorded at a high pump power density of 477 kW/cm^2 shows a narrow lasing peak at λ=371.3 nm. This peak is made up of two transition, indicated by the two Gaussian fitting curves, with the dominant transition having a linewidth of ~0.55 nm limited by the measurement system. The redshift (~0.9 nm) of the peak wavelength is partly due to bandfilling effects and also due to device heating. The variation of measured emission linewidth with pump power is shown in Fig. 8(b).
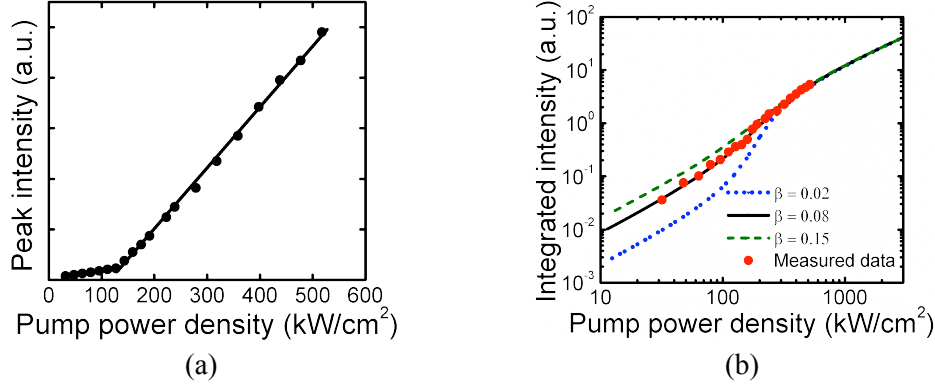
Figure 9 (a) Variation of peak output intensity with pump power (the L-L curve). The change in slope near threshold (~120 kW/cm2) is clearly observed; (b) log-log plot of spectrally integrated light intensity (red circles) versus pump power density. Theoretically calculated light intensity using the rate equations is also shown for spontaneous emission factors (β) of 0.02, 0.08, and 0.15. From a comparison of measured data with the calculated ones, a value of β ~0.08 is estimated.

The measured variation of the peak intensity of the emitted light with pump power density is shown in Fig. 9(a). A lasing threshold is observed at a pump power density of~120 kW/cm^2. Calculated plots of emission intensity versus pump power density on a log-log scale are shown in Fig. 9(b). Calculations were done for values of the spontaneous emission factor β of 0.02, 0.08 and 0.15. The material parameters for GaN were obtained from Ref. 31. The optical gain was approximated by a linear model, $g(n)=g_0(n-n_{tr})$, where $g_0=2.5\times10^{-16}$ cm^2 and $n_{tr}=7.5\times10^{18}$ cm^{-3}. The measured integrated emission intensity versus pump power density is also plotted alongside the calculated curves. The best agreement between calculated and measured data is obtained for $\beta=0.08$.

3. Coherent and Directional Emission at 1.55 μm from PbSe Colloidal Quantum Dot Electroluminescent Device on Silicon

We demonstrate electrically injected coherent and directional emission at ~1.55 μm from PbSe QDs by embedding the light emitting region between highly reflective distributed Bragg reflector (DBR) and a metal mirror, fabricated on (001) silicon substrate. The device heterostructure is schematically shown in Fig. 10(a). The light emitting region consists of PbSe QD layers, an indium tin oxide (ITO) with poly(3,4-ethylenedioxythiophene) poly(styrenesulfonate) (PEDOT:PSS) as a hole transporting layer (HTL), and ZnO nanocrystals as an electron transporting layer (ETL), similar to an excitonic solar cell structure. PbSe QDs are synthesized by a non-coordinating solvent technique and 6 nm size of PbSe QDs are chosen for 1.55 μm emission. Ethanedithiol (EDT) treatment on PbSe QDs was employed to increase the electronic coupling between PbSe QDs by displacing long chain oleate ligand.

PEDOT:PSS provides a smoother surface for ITO, which prevents morphologically induced electrical shorts and allows holes to be efficiently injected into the PbSe QDs. ZnO nanocrystals are also chemically synthesized by hydrolysis and condensation of zinc acetate dihydrate by potassium hydroxide in ethanol and treated by ultraviolet (UV) light to enhance the conductivity, which is known to passivate electron traps on the ZnO surfaces. The measured absorbance spectrum shows a shoulder peak

8

around 320 nm, corresponding to the bandgap energy of 3.9 eV. This in turn gives an average particle size of 3.5 nm. ZnO nanocrystals are inherently n-type and, therefore, serves as an efficient ETL. The injected carriers form excitons in the QD layer, leading to recombination and light emission.
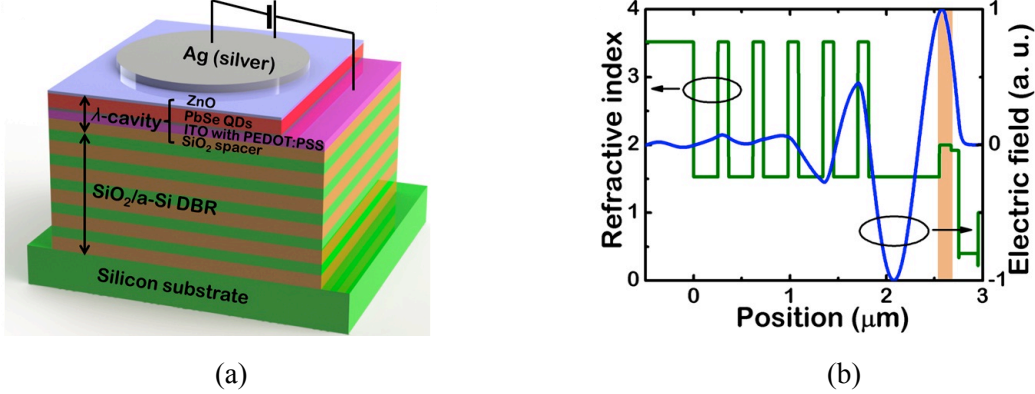

(a)   (b)

Figure 10 (a) Schematic of the device heterostructure fabricated on silicon substrate; (b) numerically calculated electric field intensity (blue line) in the device with refractive index profile (green line). The maximum electric field spatially coincides with a layer of PbSe QDs, which is highlighted.

In order to tune a resonance wavelength, 100-500 nm thick SiO_2 is additionally inserted between ITO and DBR, which tailors the cavity length from $\lambda/2$ to λ. The 5-period highly reflective bottom DBR deposited on silicon substrate is composed of amorphous silicon (a-Si) as the high refractive index layer ($n_r \sim 3.48$) and SiO_2 as the low refractive index layer ($n_r \sim 1.52$). The top mirror is formed by a layer of Ag instead of Al to attain a higher reflectivity for near infrared light. Measured reflectivity spectrum of DBR and Ag mirror exhibits a very high reflectivity of ~98.7 % at $\lambda \sim 1.55$ μm. The bandwidth of the photonic stopband spans the wavelength range of 1.3-1.6 μm due to a large index difference between a-Si and SiO_2. This avoids the Bragg mode overlap with the QD emission and ensures single mode operation.

The Q factor of the λ-cavity device calculated with the measured reflectivity of DBR and Ag mirror is about 500. Figure 10(b) shows the electric field calculated by finite difference time domain (FDTD) method with the refractive index profile shown. In order to account for the dispersive property of the metal, the dielectric function of Ag is modeled as a sum of Lorentzian functions. The maximum electric field spatially coincides with a layer of PbSe QDs, which is highlighted in this figure, and the calculated overlap of the electric field in a cavity with the PbSe QD layer is 20 %.

The current density-voltage (*J-V*) characteristics of the fabricated device were measured at room temperature. Figure 11(a) shows the measured *J-V* characteristic in a log-log plot. The slope of the plot increases around 2.3 V, which is believed to be the onset of electron and hole injection into the QDs. The current below the onset is limited by space-charge-limited conduction and therefore does not contribute to charge injection into the quantum dots. A decrease of the *J-V* slope is observed as the bias is increased above 5 V, which indicates that the carrier injection is limited by series resistance of either the ETL or the HTL. The measured *J-V* characteristics plotted on a linear scale, including the reverse bias region, shows good rectifying behavior (inset of Fig. 11(a)).
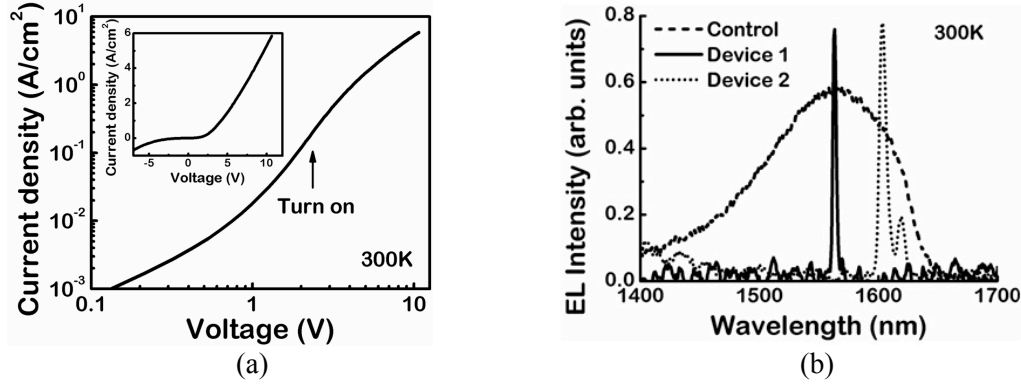
Figure 11 (a) Measured current density-voltage characteristics of the fabricated device in log-log plot. The inset shows J-V characteristics in linear scale, which exhibiting a good rectifying behavior; (b) room temperature electroluminescence spectra from the control sample without a DBR and two devices with different cavity sizes.

For electroluminescence (EL) measurements, a forward bias was applied between the ITO anode and the Ag cathode. In order to avoid heating, a pulsed current source was used with a repetition rate of 50 Hz and a duty cycle of 50 %. The light output from the device was analyzed with a high-resolution monochromator and detected with a liquid nitrogen cooled Ge detector using phase lock-in amplification. Figure 11(b) shows the normalized EL spectra of a control device without DBR and devices with DBR. The output spectrum of the control device exhibits a broad emission between 1.4-1.65 μm, with a full-width-at-half-maximum (FWHM) of ~120 nm. On the other hand, the devices with DBR and two different thickness of SiO_2 spacer show cavity resonances at λ=1563.1 (Device 1) and 1603.7 nm (Device 2), respectively. The narrowest linewidth observed is ~3.1 nm at an injection current density of 3 A/cm^2 from Device 1, which is ~38 times less than that of the control device and corresponds to a cavity Q factor of 500. The additional peak at λ=1619.3 nm was also observed on the shoulder of the dominant peak in Device 2. This abnormal peak is due to the non-uniform cavity thickness.
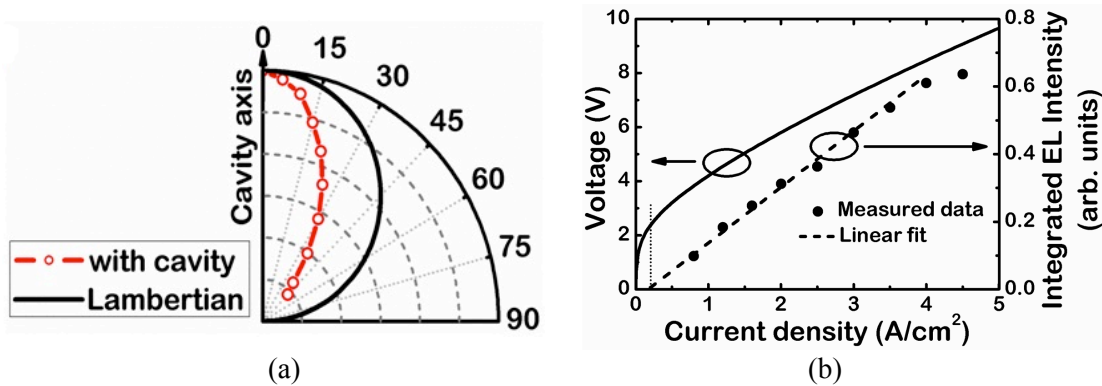

Figure 12 (a) Angular emission characteristics recorded from the device with DBR at angles ranging from 0-45 degrees with respect to the cavity axis. The Lambertian pattern is also shown for comparison; (b) measured voltage-current density and light-current density characteristics of the device. The integrated light output increases linearly with current. The extrapolation of the linear fit indicates a turn-on voltage of ~2.4 V.

10

The light emission from the device with DBR was also measured at angles ranging from 0-45 degrees with respect to the cavity axis, as shown in the angular emission characteristics (Fig. 12(a)). Also shown is the Lambertian emission pattern for comparison. The device with DBR exhibits a highly directional light output parallel to the cavity axis, showing a smaller divergence compared to the Lambertian emission pattern. The measured light-current density characteristics shown in Fig. 12(b) displays the linear increase of light output as the current density increases. The onset of light output inferred from the extrapolation of the linear fit to the measured points is around 2.4 V, which coincides with the turn-on estimated from the *J-V* characteristics. As the current density increases above 4 A/cm^2, the integrated light output becomes saturated due to heating.

4. Effect of Magnetic field and Modulation Doping on Polariton Emission Characteristics of a Multiquantum-Well Microcavity Diode

Strong coupling between quantum well (QW) excitons and photons confined in a microcavity leads to the creation of polaritons which are bosons. Although polariton condensation and room temperature coherent polariton emission have been demonstrated in various material systems, the excitation of QW excitons was achieved via optical pumping. For device applications, it is necessary to demonstrate polariton condensation and coherent emission with non-resonant electrical injection, which still remains a challenge.
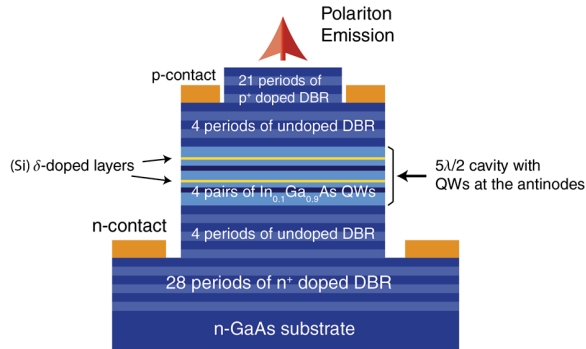

Figure 13 Schematic representation of fabricated GaAs-based modulation doped quantum well-microcavity diode with 4 pairs of In0.1Ga0.9As / GaAs quantum wells.

The microcavity device used in this study, shown in Fig. 13, was grown by molecular beam epitaxy on a n-doped GaAs (001) substrate and consists of an undoped (n~10^{15} cm^{-3}) 5λ/2 GaAs cavity surrounded by 32 periods of Si-doped (n = 2 × 10^{18} cm^{-3}) GaAs / Al$_{0.85}$Ga$_{0.15}$As forming the bottom distributed Bragg reflector (DBR) and 25 periods of Be-doped (p = 4 × 10^{18} cm^{-3}) GaAs / Al$_{0.85}$Ga$_{0.15}$As forming the top DBR. Four periods of the DBR adjoining the cavity on both sides were left undoped to minimize doping related losses. Four pairs of undoped 10 nm In$_{0.1}$Ga$_{0.9}$As/10 nm GaAs QWs are grown at the antinodes of the cavity photon field to maximize the interaction between the QW excitons and the cavity photons. A 1 nm thick region at a distance of 10 nm below each pair of QWs was Si-doped n-type. Three samples were investigated with Si-doped concentration of n = 0, 1x10^{17} cm^{-3} and 2x10^{17} cm^{-3} respectively. Since at these levels the modulation doping is highly degenerate, the impurity band overlaps with the conduction band and the dopants require no energy for ionization and thus the corresponding thermally ionized electron sheet densities are n$_e$ = 0, 1x10^{10} and 2x10^{10} cm^{-2} for the 3 samples. Standard photolithography and wet chemical etching techniques were employed to form a mesa of 50 µm diameter. Ring-shaped annular Pd/Zn/Pd/Au p-contact and Ni/Ge/Au/Ti/Au n-contact were formed, for hole and

electron injection, respectively, to complete device fabrication. The contacts were deposited on the first doped Bragg pair to minimize Joule heating.
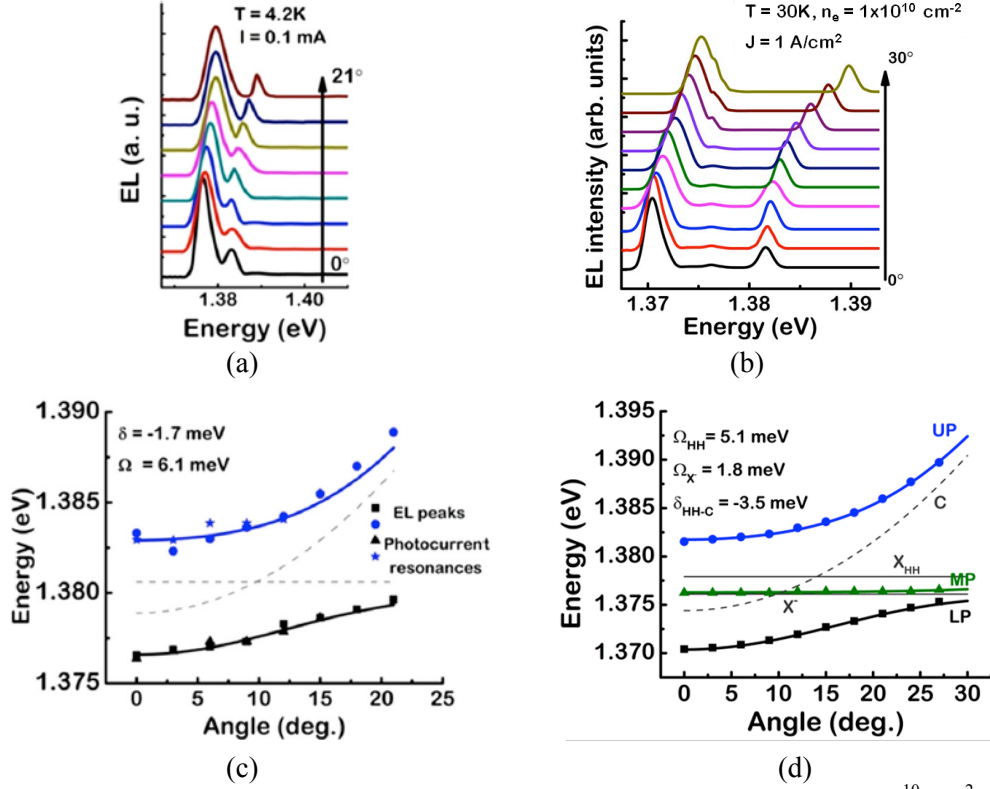

(a)

(b)

(c)

(d)

Figure 14 (a) and (b) Angle-resolved electroluminescence at 30K from = 0 (a) and 1×10^{10} cm^{-2} (b); (c) and (d) polariton dispersion curves obtained from (a) and (b), respectively. The solid curves represent the polariton dispersions calculated from a coupled harmonic oscillator model.

The dispersion of the resonant modes was measured at 30K by angle resolved electroluminescence, with an angular resolution of 1°, at an injection current density of 0.8 A/cm^2 with a high resolution monochromator (spectral resolution ~ 0.03 nm) and detected with a photomultiplier using phase sensitive lock-in amplification. The measured spectra for the samples with undoped and modulation doped (sheet electron density of $n_e = 1\times10^{10}$ cm^{-2}) are shown in Figs. 14(a) and (b), respectively. Both samples show two distinct polariton peaks, with the LP peak asymptotically approaching the exciton energy at larger angles. In a modulation doped sample, signature of a weak middle polariton (MP) branch is also observed, which has been attributed to the effect of charged excitons or trions (X$^-$). The resonances obtained from the electroluminescence spectra are plotted in Figs. 14(c) and (d) together with the calculated dispersion curves (solid lines) of the upper polariton (UP), MP and lower polariton (LP) branches by using the one-to-one correspondence between the emission angle of the out-coupled photons and the in-plane wave number of the polaritons. The interaction between the cavity and exciton modes was modeled with a coupled harmonic oscillator Hamiltonian. Only the interaction between the cavity photon and the heavy-hole exciton is considered because the light-hole exciton transition is energetically situated 15 meV above the hh-exciton transition due to biaxial strain in the quantum wells. For undoped sample, a Rabi splitting of 6.1 meV and a negative detuning δ of -1.7 meV are derived. In a modulation doped

one, the measured results exhibit excellent agreement with the interaction potentials of the heavy-hole exciton with the cavity mode V_{Xhh} = 5.1 meV and trion with the cavity mode V_{X-} = 1.8 meV and a cavity to heavy-hole exciton detuning δ of -3.5 meV.

In order to determine the effect of the polariton-electron scattering in suppressing the bottleneck and enhancing the rate of polariton relaxation to the $k_{\parallel} \sim 0$ states, we have calculated the polariton occupancy in k-space as a function of n_e from the measured angle-resolved electroluminescence data at an injection current density of 4A/cm^2 by using the formula, $I_{LP}(k_{\parallel}) = \eta N_{LP}(k_{\parallel}) \, | \, C(k_{\parallel}) \, |^2 \, M / \tau_C$, where η is the collection efficiency, $\tau_C / |C(k_{\parallel})|^2$ is the radiative lifetime of the LPs, M is the number of transverse states included in the detection cone and $|C(k_{\parallel})|^2$ is the photon fraction at a wave-vector $k_{\parallel}$. The number of states within the detection cone is given by $M = D^2 (k_0 \Delta\theta)^2 / 16$, where D is the diameter of the emission spot, $k_0 = 2\pi/\lambda$ and $\Delta\theta$ is the detection half angle. τ_C is estimated from the cavity Q, and the value of η is estimated by replacing the sample with a source of known power (Ti:sapphire laser with suitable attenuation). The LP number density per k-state is plotted in Fig. 15. A pronounced relaxation bottleneck at $k_{\parallel} \sim$ 1.17×10^4 cm^{-1} is observed for the sample with n_e = 0. However for samples with n_e = 1×10^{10} and 2×10^{10} cm^{-2}, the population of the ground state increases, while the reservoir population remains almost unchanged, and the bottleneck is removed.
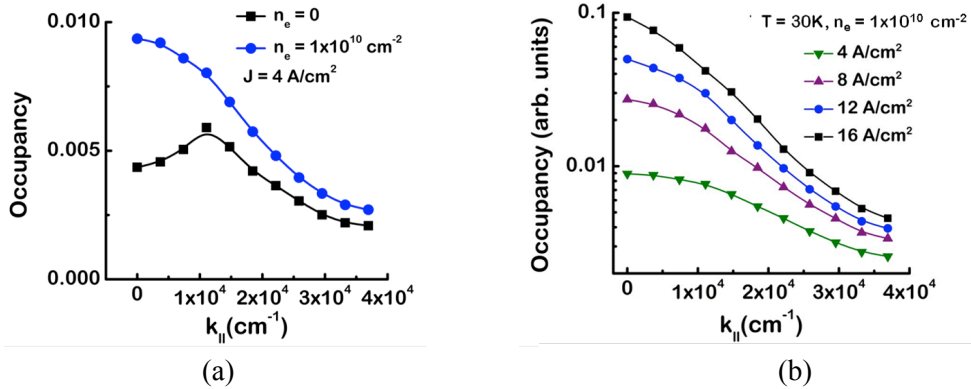

Figure 15 (a) Occupancy of lower polariton branch (LPB) as a function of in-plane wave vector for different modulation doping density (n_e = 0 and 1×10^{10} cm^{-2}) obtained from angle-resolved electroluminescence; (b) occupancy of LPB for various injection currents at T = 30K in a device with doping density n_e = 1×10^{10} cm^{-2}.

To investigate the dependence of occupation of different k-states on injected current density and the possibility of polariton condensation, we measured the angle-resolved electroluminescence at 30K for the sample with n_e = 1×10^{10} cm^{-2}. The data are shown in Fig. 15(b). At low injection densities, as mentioned earlier, a distribution without any bottleneck is observed with comparable occupancies between $k_{\parallel}$ = 0 and 1.23×10^4 cm^{-1}. At higher injection currents, the occupancy of the ground state shows a super-linear increase, while that of the reservoir shows very little increase. Although a bimodal distribution (with a massively occupied ground state) associated with polariton lasing is not observed, the occupancy profile can be characterized by the Maxwell-Boltzmann distribution: N = N$_0$exp(-(E(k)-E(0))/kT), (where E(k) is the LP energy at $k_{\parallel}$

and N_0 is the occupancy at $k_{\parallel} = 0$). It is evident that polariton-electron scattering plays a role similar to polariton-phonon scattering and thermalizes the LP distribution.

As an alternative way to suppress the bottleneck, we have applied a magnetic field on the undoped sample. The LP number density per k-state is plotted in Fig. 16. A pronounced relaxation bottleneck is observed at low injection current densities for zero magnetic field, with the bottleneck persisting at higher injection levels for low magnetic fields. On the other hand, a distribution with an increase in occupancy near $k_{\parallel} \sim 0$ with complete suppression of the bottleneck evolves for a field > 5 Tesla. Figure 16(b) illustrates the occupancy as a function of current injection for B = 7 Tesla. At low injection, the occupancy is comparable at all in-plane wave vectors with no observable relaxation bottleneck. At high injection levels, the occupancy of the ground state shows a non-linear increase, while that of the reservoir remains fairly constant. In seeking an explanation for the suppression of the relaxation bottleneck with the magnetic field, we have calculated the relative polariton-acoustic phonon and polariton-polariton scattering rates into the $k_{\parallel} \sim 0$ state. Application of a magnetic field parallel to the growth direction increases the exciton binding energy and decreases the 2D Bohr radius. This causes an increase in the exciton oscillator strength which in turn increases the Rabi splitting. Furthermore, for a fixed negative detuning, an increase in the Rabi splitting increases the exciton fraction and the density of states of the LP modes. Since the polariton-phonon scattering rates are proportional to the density of states of the polariton modes at the scattering energy, the exciton fraction of the initial and the final states, and overlap integrals between the excitons in the quantum wells and the phonons in the bulk, an increase in the Rabi splitting with increasing magnetic field should enhance the rates (for the same detuning).
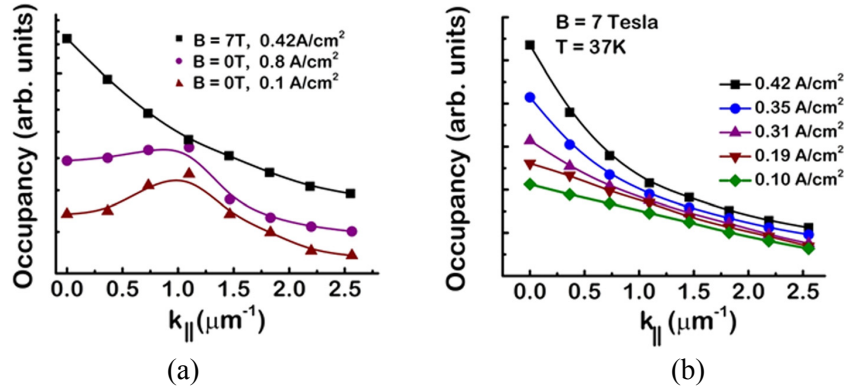

Figure 16 (a) Occupancy of LPB as a function of in-plane wave vector for different magnetic fields and injection currents obtained from angle-resolved electroluminescence; (b) occupancy of LPB for various injection currents at B=7 Tesla.

Finally, the dependence of light output on the injection current density was investigated by measuring the electroluminescence at $k_{\parallel} \sim 0$ as a function of injection current (pulsed to avoid device heating). With increasing current density the UP and LP polariton peaks progressively come closer in energy (Fig 17(a)) and merge into a single emission line, signaling the transition to the weak coupling regime. As the current density increases, linewidth narrowing of the LP emission is not observed. The integrated electroluminescence from the lower polaritons was measured as a function of injection current density and the data are shown in Fig. 17(b). The LP densities shown in this

figure and that quoted above are calculated from the injection current density by using the relation $n_{LP} = \eta_i J\tau/q$, where η_i is the internal quantum efficiency, J is the current density and τ is the exciton lifetime. We have assumed $\eta_i = 1$ and an estimated exciton lifetime of 0.75 ns. In the absence of polariton-electron scattering ($n_e = 0$), the intensity grows linearly with injection, which is a signature of polariton-phonon scattering. In contrast, in the presence of such scattering, the measured intensity grows super-linearly with increasing current density (in agreement with the increase in polariton occupation at $k_\parallel \sim 0$). A quadratic increase in the LP emission intensity is observed in a small range of current density (15 A/cm^2 $\leq$ J$\leq$ 22 A/cm^2). The observed super-linear dependence on current is attributed to enhanced relaxation of LPs due to polariton-electron scattering, in agreement with the data of Fig. 15(a). The quadratic dependence at the highest injection current densities suggests that the relaxation in this regime is dominated by polariton-polariton scattering.
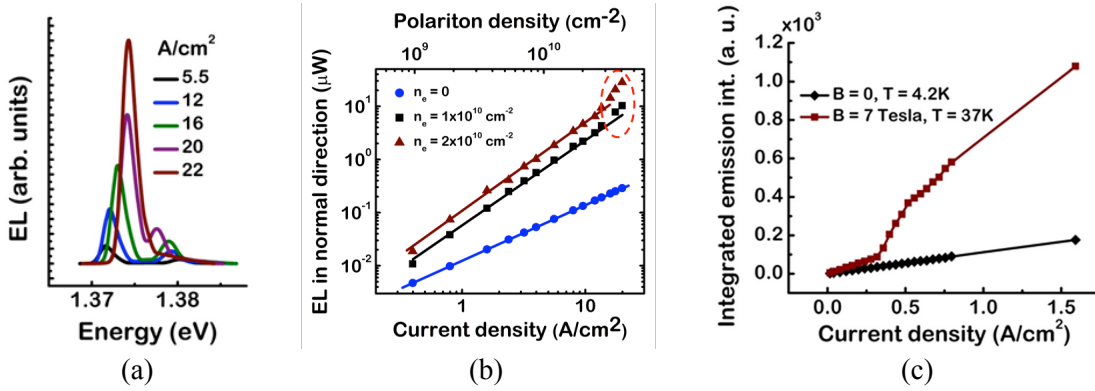

(a)   (b)   (c)

Figure 17 (a) LP and UP electroluminescence spectra as a function of injection current density in a device with doping density $n_e = 1\times10^{10}$ cm^{-2}; (b) output power measured in the normal direction versus injection current density for $n_e = 0, 1\times10^{10}$ cm^{-2} and 2×10^{10} cm^{-2}; (c) integrated emission intensity measured in the normal direction versus injection current density at 0 and 7 Tesla.

However, a distinct non-linearity appears in the light-current characteristics with application of magnetic field in an undoped sample (Fig. 17(c)). At 7 Tesla, the threshold of the non-linearity is at 0.32 A/cm^2, well within the strong coupling regime. We believe that the observed non-linearity is also related to the enhanced polariton-phonon scattering rates and a suppression of the relaxation bottleneck in the presence of a magnetic field, leading to a faster relaxation of the LPs down to $k_\parallel \sim 0$ and a subsequent enhancement of the electroluminescence in the normal direction. The polariton density at the non-linear threshold was estimated to be in the range of $\sim(2.4–3)\times10^9$ cm^{-2}. This value is a factor of 8 smaller than the critical density for the Kosterlitz-Thouless (KT) transition at which a perfect Bose-Einstein condensate (BEC) at thermal equilibrium is formed. However, a non-equilibrium condensate of finite size, which may be formed at threshold will account for the lower value of polariton density.

Archival publications (published) during reporting period:

1. A. Das, B. Xiao, S. Bhowmick, and P. Bhattacharya, "Polariton Emission Characteristics of a Modulation-Doped Multiquantum-Well Microcavity Diode," *Appl. Phys. Lett.* accepted (2012).

2. P. Bhattacharya, A. Das, S. Bhowmick, M. Jankowski, C.-S. Lee, "Effect of magnetic field on polariton emission characteristics of a quantum-well microcavity diode," *Appl. Phys. Lett.* 100, 171106 (2012).

3. J. Heo, S. Bhowmick, and P. Bhattacharya, "Threshold Characteristics of Quantum Dot Rolled-up Microtube Lasers," *IEEE J. Quantum Electron.* **48**, 927 (2012).

4. J. Heo, Z. Jiang, J. Xu, and P. Bhattacharya, "Coherent and directional emission at 1.55 μm from PbSe colloidal quantum dot electroluminescent device on silicon," *Opt. Exp.* **19**, 26394 (2011).

5. J. Heo, W. Guo, and P. Bhattacharya, "Monolithic single GaN nanowire laser with photonic crystal microcavity on silicon," *Appl. Phys. Lett.* **98**, 021110 (2011).

6. W. Guo, M. Zhang, A. Banerjee, and P. Bhattacharya, "Catalyst-Free InGaN/GaN Nanowire Light Emitting Diodes Grown on (001) Silicon by Molecular Beam Epitaxy," *Nano Lett.* **10**, 3355 (2010).

Conference Presentations:

1. J. Heo, S. Bhowmick, and P. Bhattacharya, "Threshold condition and modal gain of rolled-up microtube lasers," *CLEO 2012*, San Jose CA, May 2012.

2. P. Bhattacharya, A. Das, M. Jankowski, S. Bhowmick, C. S. Lee, and S. Jahangir, "Electrically injected polariton lasing from a GaAs-based microcavity under magnetic field," CLEO 2012, San Jose CA, May 2012.

3. W. Guo, J. Heo, M. Zhang, and P. Bhattacharya, "Monolithic single GaN nanowire laser with photonic crystal microcavity on silicon," *International Workshop on Nitride semiconductors 2010*, Tampa FL, September 2010.

4. M. Zhang, W. Guo, A. Banerjee, and P. Bhattacharya, "InGaN/GaN nanowire green light emitting diodes on (001) Si substrates", *Device Research Conference*, June 2010.

5. W. Guo, J. Heo, D. Basu, P. Bhattacharya, and Z. Mi, "Light Emission Characteristics of Silicon-Based Self Rolled-Up Micro(Nano)-Cavity with

InAs/GaAs Quantum Dot Heterostructures," *NAMBE 2009*, Princeton NJ, August 2009.

Awards and honors during reporting period:

1. Professor P. Bhattacharya received the Heinrich Welker Prize in 2010.